Decoupling Model Predictive Controlled Three-Level Noninverting Buck–Boost Converter Applied in DC Energy Storage System

Kaitao Bi, Cheng Xu, Jian Ai, Jianfei Li, and Qigao Fan, *Senior Member, IEEE*

***Abstract*—To solve the bidirectional power control issue under wide range voltage changes on both sides of the dc bus and energy storage battery in the dc energy storage system, this article proposes a multiobjective decoupling model predictive control (MPC) (MOD-MPC) strategy for the three-level noninverting Buck–Boost converter (TLNBC). The mathematical model of TLNBC based on the voltage difference of split capacitors is first studied, solving the problem of multi branch modeling of split capacitor voltage. On this basis, a MOD-MPC power control strategy with dual-carrier modulation method is proposed by analyzing the relationship between system current and split capacitor voltage sharing control. The optimal control variables solution is directly obtained by solving the cost function, achieving independent control of system current and split capacitor voltage sharing, and greatly reducing computational load. The decoupling MPC controlled TLNBC can operate in Buck and Boost modes when energy is transmitted in any direction catering to various scenarios while exhibiting favorable control performance. The effectiveness of the converter and control strategy is verified through experiments.**

***Index Terms*—Bidirectional power control, decoupling model predictive control strategy, photovoltaic energy storage system, three-level noninverting buck–boost converter.**

I. Introduction

RENEWABLE energy, represented by photovoltaics and wind power, is gradually becoming the primary source of energy in human society [1], [2], [3]. However, the inherent volatility and intermittency of renewable energy pose a significant challenge to the stability of power grid. Energy storage technology is an effective solution to address these issues [4]. In recent years, electrochemical energy storage, as a representative form of energy storage technology, has drawn a lot of attention.

Energy storage system (ESS) can be divided into two types based on their location in the power grid: Ac ESS and dc ESS [5], [6]. Dc ESS is commonly used in photovoltaic (PV) generation systems, and the typical grid architecture is shown in Fig. 1 [7]. The batteries are connected to the dc bus through a bidirectional dc–dc converter. However, due to the power fluctuations in PV systems, the converter needs to be capable of converting energy with Buck or Boost conversion, regardless of the direction of energy flow. The four-switch bidirectional dc–dc converter is often employed in low-voltage dc ESS [8]. Considering the constraints of voltage stress, the three-level topology represented by flying-capacitor (FC) and half-bridge (HB) topologies is often used in the medium and high voltage dc ESS [9], [10]. Bi et al. [11] proposed an MPC strategy for FC topology applied in dc energy storage system. The dynamic regulation of flying capacitor voltage and the precharging issue result in heightened system control complexity and diminished reliability. In contrast, the HB topology studied in [12] features a more concise topology and control requirements. Manandhar et al. [13] applied the HB three-level converter in the dc ESS and studied the basic control principle. Additionally, the HB three-level bidirectional converter has been applied in a megawatt-level electric vehicle dc charging station [14]. Overall, the HB three-level topology exhibits more pronounced advantages in terms of both topology structure and system control when compared to the FC three-level topology.

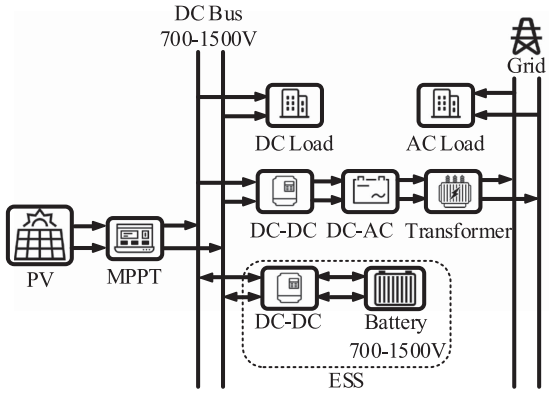

Fig. 1. Grid architecture based on energy storage system on DC side.

In addition to the voltage level, the dc bus and the energy storage battery share the same voltage variation range, as depicted in the grid architecture shown in Fig. 1, which poses higher

Manuscript received 18 September 2023; revised 10 January 2024; accepted 8 February 2024. Date of publication 23 February 2024; date of current version 19 April 2024. This work was supported in part by the Natural Science Foundation of Jiangsu under Grant BK20200623 and in part by the Natural Science Foundation of China under Grant 62373168. Recommended for publication by Associate Editor M. J. Scott. *(Corresponding author: Qigao Fan.)*

Kaitao Bi and Cheng Xu are with Jiangnan University, Wuxi 214122, China.

Jian Ai is with the Department of Automation Engineering, Southeast University, Nanjing 211102, China.

Jianfei Li is with the Sineng Electric Company Ltd., Jiangsu 214443, China.

Qigao Fan is with the School of IOT Engineering, Jiangnan University, Wuxi 214122, China (e-mail: qgfan@jiangnan.edu.cn).

Color versions of one or more figures in this article are available at https://doi.org/10.1109/TPEL.2024.3367903.

Digital Object Identifier 10.1109/TPEL.2024.3367903

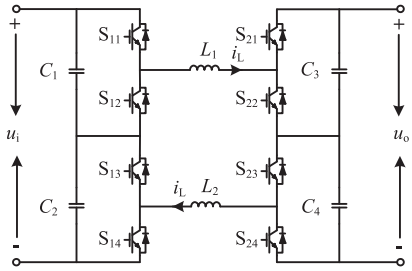

Fig. 2. Topology of TLNBC.

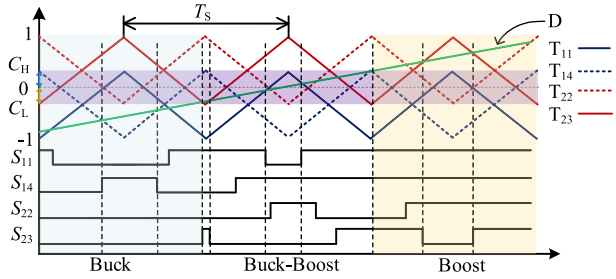

Fig. 3. Schematic diagram of dual-carrier modulation.

power conversion requirements for the dc–dc converters applied in ESS. When energy is transferred in any direction, the dc–dc converter may operate in either Buck or Boost mode to meet the power conversation requirements under dual-end voltage variations. In order to solve this issue, Bi et al. [15] proposed a single carrier modulation method to make the converter always work in Buck–Boost mode. Ghias et al. [16] proposed a single-carrier phase-shift modulation strategy to realize Buck–Boost operation within the entire voltage gain range. However, both strategies increase system losses. To address this issue, Bai et al. [17] proposed a complex yet efficient hybrid pulse width modulation (PWM) strategy for the four-switch topology, enabling smooth control of the output voltage during mode changes and eliminating the impact of dead time on control performance. Aharon et al. [18] proposed a dual-carrier modulation strategy for the four-switch topology, achieving smooth mode control in Buck, Buck–Boost, and Boost modes while minimizing current ripple caused by dead time.

In addition, the dynamic performance of ESS is crucial for ensuring the stability of dc bus. Proportional integral (PI) algorithm as the traditional control method is often used in dc–dc converters [19]. However, the output gain of the PI algorithm is controlled through local linearization, resulting in inconsistent global control performance, which poses challenges in achieving the desired dynamic response under nonlinear loads. Model predictive control (MPC) as a powerful nonlinear control scheme is gradually replacing traditional PI algorithm [20], [21], [22]. In [23], the application of finite control set MPC strategy in dc–dc converters improved system dynamic performance. However, the varying switching frequency reduces system efficiency. Chen et al. [24] studied the fixed frequency MPC control scheme for FC dc–dc converters. Nevertheless, it requires multiple mathematical iterations to derive the optimal duty ratio, and the coupling relationship between multiple control objectives makes it difficult to design weight factors, increasing computational load and failing to achieve optimal system performance.

In the dc ESS, the bus and battery display a comparable range of voltage variations, which requires the dc–dc converter in the ESS to have fast response speed and energy transfer ability under wide range voltage variation at both ends. Therefore, this article proposes a multiobjective decoupling MPC (MOD-MPC) strategy based on dual-carrier modulation for the three-level noninverting Buck–Boost converter (TLNBC). The dual-carrier modulation method is employed by TLNBC to achieve smooth mode changing when the voltage of the dc bus and energy storage battery changes. A simplified mathematical model of TLNBC based on split capacitor voltage difference is proposed, which reduces the modeling complexity of TLNBC under the requirements of system current and split capacitor voltage control. On this basis, the MOD-MPC strategy based on dual-carrier modulation was proposed, achieving decoupling control of system current and split capacitor voltage. And, the cost function is optimized to reduce the computational load. The experimental results show that the proposed MOD-MPC can effectively control the system current and split capacitor voltage on both sides, and can effectively satisfy the power control requirements of dc ESS.

The rest of this article is organized as follows. Section II analyzes the TLNBC and its working principle with dual-carrier modulation. In Section III, a simplified mathematical model and MOD-MPC strategy for TLNBC are proposed. Section IV validates the proposed control strategy effectively using the dc ESS experimental platform. Finally, Section V concludes this article.

II. Basic Principle Analysis of TLNBC

A. Basic Working Principle

Fig. 2 shows the TLNBC topology suitable for ESS on dc side, which achieves three-level output through half-bridge stacking. The H structure of the converter enables it to operate in multiple modes during unidirectional energy flow. C_1–C_4 represent the split capacitors, while L_1 and L_2 represent the inductors.

The TLNBC can operate with three different modes: Buck, Buck–Boost, and Boost, regardless of the direction of energy flow. Taking the energy flow from left to right as an example, in Buck mode, S_{11} and S_{14} are turned ON alternately, while the other switches remain OFF. In Buck–Boost mode, S_{11} and S_{14}, S_{22} and S_{23} are turned ON alternately. The carrier phases of S_{11}, S_{23}, S_{14}, and S_{22} are the same. In Boost mode, S_{11} and S_{14} are continuously turned ON, S_{22} and S_{23} are turned ON and OFF alternately. Similarly, when energy flows from right to left, it only requires control of the other four switches. The operating state of the TLNBC is determined by the voltage on both sides. To accommodate a wide voltage range, achieve favorable dynamic performance, and reduce switching losses, dual-carrier modulation method is employed by TLNBC, and the modulation principle is illustrated in Fig. 3.

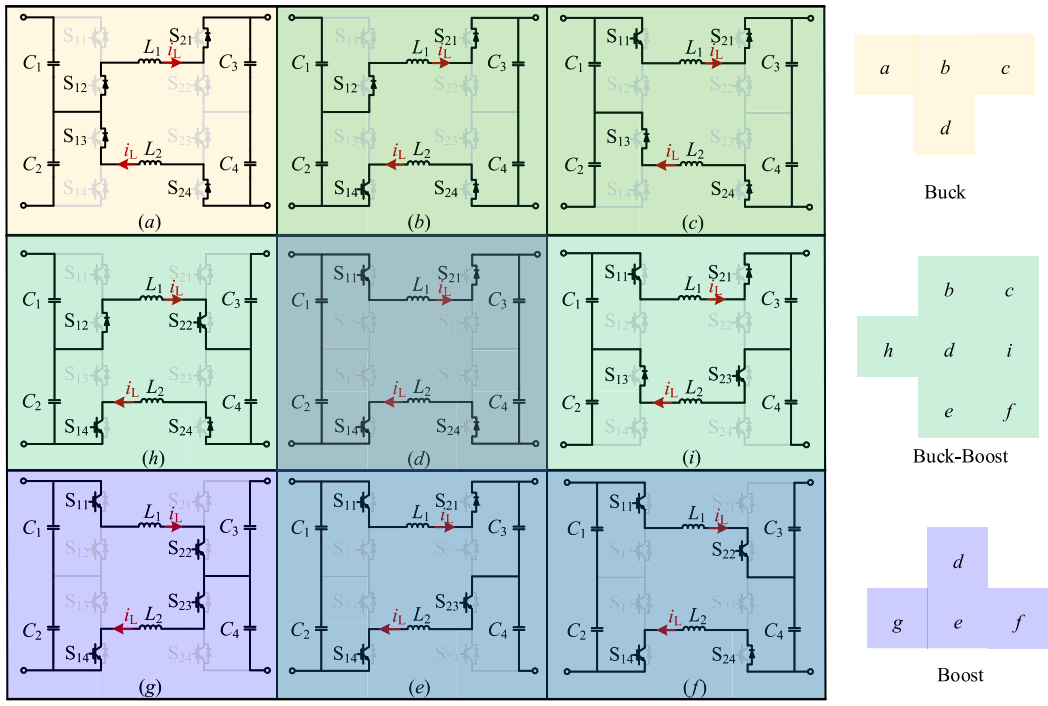

Fig. 4. Operating state circuits of TLNBC.

As shown in Fig. 3, T_s represents the switching period, T_{11}–T_{23} represent the triangular carriers of S_{11}–S_{23}, and D is the modulation signal. While C_H and C_L are the offsets based on the peak of T_{11} and T_{14}, and the valley of T_{22} and T_{23}, respectively. From Fig. 3, it can be observed that the working modes of the TLNBC can be determined by C_L and C_H. When $C_H = C_L = 0$, the converter operates solely in Buck or Boost mode. When $C_H > C_L$ and $D > C_H$, the converter operates in Boost mode. When $C_L \le D \le C_H$, the converter operates in Buck–Boost mode. When $D < C_L$, the converter operates in Buck mode. Based on dual-carrier modulation, TLNBC has a total of nine working states, as shown in Fig. 4. Define d_1 as the duty ratio of S_{11} and S_{14}, and d_2 as the duty ratio of S_{22} and S_{23}. Based on the duty ratio operating range depicted in Fig. 3, the expressions for d_1 and d_2 can be derived as follows:

$$d_1 = \begin{cases} 0, & D \le -1 \\ \frac{1+D}{1+C_H}, & -1 \le D \le C_H \\ 1, & D \ge C_H \end{cases},$$

$$d_2 = \begin{cases} 0, & D \le C_L \\ \frac{D-C_L}{1-C_L}, & C_L \le D \le 1 \\ 1, & D \ge 1 \end{cases}. \quad (1)$$

According to (1) and volt-second principle, the voltage gain of TLNBC with dual-carrier modulation can be expressed as

$$G(D) = \frac{u_o}{u_i} = \begin{cases} \frac{1+D}{1+C_H}, & -1 \le D \le C_L \\ \frac{(1-C_L)(1+D)}{(1+C_H)(1-D)}, & C_L \le D \le C_H \\ \frac{1-C_L}{1-D}, & C_H \le D \le 1 \end{cases}. \quad (2)$$

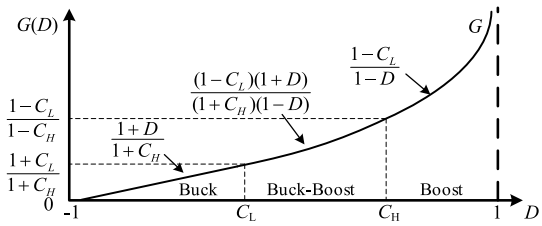

Fig. 5. Voltage gain curve of TLNBC with dual-carrier modulation.

TABLE I
CIRCUIT STATES OF TLNBC WITH DIFFERENT DUTY RATIOS

Operating mode	Duty ratio	Circuit state
Boost	$(1-M)/2 \le D \le 1$	$g\ f\ g\ e$
	$M \le D \le (1-M)/2$	$d\ f\ d\ e$
Buck—Boost	$0 \le D \le M$	$e\ d\ f\ h\ f\ d\ e\ i$
	$-M \le D \le 0$	$d\ b\ h\ b\ d\ c\ i\ c$
Buck	$(M-1)/2 \le D \le -M$	$d\ b\ d\ c$
	$-1 \le D \le (M-1)/2$	$a\ b\ a\ c$

Thus, the voltage gain curve of TLNBC can be plotted according to (2), as shown in Fig. 5. The values of C_H and C_L indicated on the horizontal axis represent the operation mode switching points. It can be seen that the voltage gain is smooth, indicating that the converter can achieve continuous mode switching.

Assuming $C_H = -C_L = M$, it can be derived from Figs. 3 and 4 that the converter operating in different modes has several different states, denoted as states (a) to (i), and the circuit states with different duty ratios are shown in Table I.

TABLE II
INDUCTIVE CURRENT RIPPLE IN STEADY STATE

Operating mode	Duty ratio	Current ripple Δi_L
Boost	$(1-M)/2 \le D \le 1$	$\frac{2D+M-1}{2(M+1)}\frac{u_i}{Lf_S}$
	$M \le D \le (1-M)/2$	$\frac{(M+D)(1-2D-M)}{2(1-D)(1+M)}\frac{u_i}{Lf_S}$
Buck–Boost	$0 \le D \le M$	$\frac{D(M-D)}{(1+M)(1-D)}\frac{u_i}{Lf_S}$
	$-M \le D \le 0$	$\frac{D(D+M)}{(1+M)(1-D)}\frac{u_i}{Lf_S}$
Buck	$(M-1)/2 \le D \le -M$	$\frac{(D-M)(1+2D-M)}{2(1+M)^2}\frac{u_i}{Lf_S}$
	$-1 \le D \le (M-1)/2$	$\frac{(1+D)(M-D)}{2(M+1)^2}\frac{u_i}{Lf_S}$

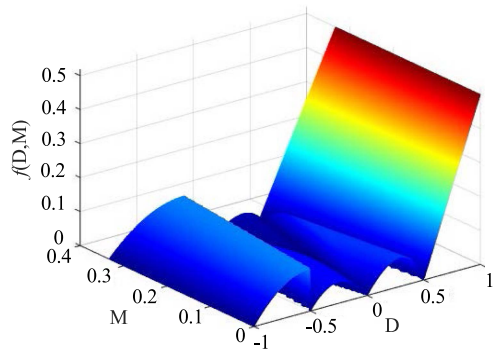

Fig. 6. Current ripple curves with different D and M.

B. Circuit Parameters

It is known that the voltage stress of the switching device in a three-level converter is half of the input voltage. According to the circuit states of TLNBC shown in Fig. 4, it can be seen that the voltage stress of each switching device in TLNBC is the split capacitor voltage in parallel at both ends of the converter. Under steady state, the split capacitor voltage is half of the port voltage. Therefore, the voltage stress of each switching device can be expressed as

$$\begin{cases} u_{S11\sim14} = \frac{u_i}{2} \\ u_{S21\sim24} = \frac{u_o}{2}. \end{cases} \tag{3}$$

Thus, it can be derived from (3) that the switching device voltage stress in TLNBC is determined by the topology and is independent of the operating mode.

According to the basic equation of inductance voltage and the working circuit states under different duty ratios shown in Table I, the inductance current ripple Δi_L under different carrier offset values can be obtained. The expressions are presented in Table II. Here, f_s represents the switching frequency, and L is the total inductance given by $L = (L_1 + L_2)$.

It can be seen from Table II that the current ripple is a function of D and M. According to Table II, the curve of inductance current ripple under different carrier offsets can be plotted, as shown in Fig. 6.

As shown in Fig. 6, the current ripple reaches the maximum value when $D = 1$ and is not related to the carrier offset. The expression for the maximum current ripple is shown in (4). Thus, the inductance parameters can be designed based on the maximum system voltage and switching frequency

$$L_{1\_\min} = L_{2\_\min} \ge \frac{u_i}{2\Delta i_{L\_\max} f_s}. \tag{4}$$

Due to the symmetrical structure, split capacitors have the same capacitance value. Taking the output side as an example, the output voltage ripple is the superposition of voltage ripple of C_3 and C_4. In a series structure, the maximum capacitor voltage ripple value is the same as that of a single capacitor's voltage ripple. Furthermore, the charging or discharging of split capacitor is determined by the operating state of TLNBC. Taking C_3 and C_4 as the example, in Buck–Boost or Boost mode, when TLNBC switches from state (e) to state (d), C_4 is charged. In contrast, when TLNBC switches from state (b) to state (d) in Buck mode, C_4 is neither charged nor discharged. Therefore, based on similar analysis and combined with Fig. 4 and Table I, it can be seen that C_3 and C_4 are only charged or discharged in Buck–Boost and Boost modes. According to the basic capacitance equation, the expressions for the minimum values of C_3 and C_4 under maximum voltage ripple are shown in

$$C_{\min} \ge \frac{u_o}{Rf_s\Delta u_{c\_\max}}\frac{D+M}{1+M} \tag{5}$$

where R represents the load value. Considering the symmetric topology, (5) is also applicable for designing C_1 and C_2, and is not be repeated. And, it can be seen from (5) that TLNBC has the maximum voltage ripple when $(D+M)/(1+M)$ approaches 1.

III. MULTIOBJECTIVE DECOUPLING MPC STRATEGY

With the aid of the dual-carrier modulation method, TLNBC can operate in Buck, Buck–Boost, and Boost modes. When applying TLNBC in an ESS, it is essential to control the inductance current and split capacitor voltage, and ensure seamless switching of the operating mode during energy conversion. Thus, the proposed MPC strategy is designed based on these requirements.

A. Mathematical Model of TLNBC Based on Split Capacitor Voltage Difference

The conventional modeling method for balancing split capacitor voltage and controlling system current uses capacitor voltage and inductance current as control variables. However, for the TLNBC topology, due to the split capacitor being directly connected to the dc bus or batteries, there are multiple charging and discharging circuits, making it difficult to model the converter directly using the capacitor voltage as a variable. Taking the input side as an example, the charging and discharging state of the split capacitor is derived based on midpoint a, as shown in Fig. 7, where $\Delta u_{C12} = u_{C1}$-u_{C2}.

Since C_1 and C_2 have the same capacitance, the voltage difference between u_{C1} and u_{C2} remains constant when they

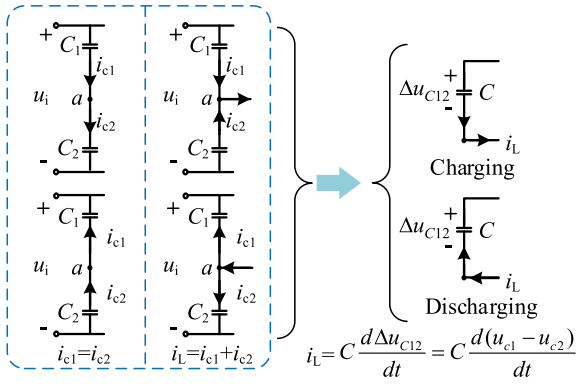

Fig. 7. Equivalent voltage variation law of series split capacitors.

TABLE III
OPERATING TIME OF DIFFERENT CIRCUIT STATES

Buck Mode		Boost Mode	
State	Operating time	State	Operating time
a	(0.5-0.5(d_{11}+d_{14}))T_S	*d*	(0.5-0.5(d_{22}+d_{23}))T_S
b	$d_{14}T_S$	*f*	$d_{22}T_S$
a	(0.5-0.5(d_{11}+d_{14}))T_S	*d*	(0.5-0.5(d_{22}+d_{23}))T_S
c	$d_{11}T_S$	*e*	$d_{23}T_S$
Buck–Boost Mode			
State	Operating time	State	Operating time
d	(d_{11}+d_{14})-0.5)T_S	*d*	(d_{11}+d_{14})-0.5)T_S
b	(0.5-0.5(d_{11}+d_{22}))T_S	*c*	(0.5-0.5(d_{14}+d_{23}))T_S
h	$d_{22}T_S$	*i*	$d_{23}T_S$
b	(0.5-0.5(d_{11}+d_{22}))T_S	*c*	(0.5-0.5(d_{14}+d_{23}))T_S

are charged or discharged simultaneously. However, when the charging and discharging states of C_1 and C_2 differ, it generates a current through the inductance, causing a deviation in u_{C1} and u_{C2}. Therefore, in order to achieve voltage balancing control, the voltage difference Δu_{C12} on the input side, as shown in Fig. 7, is used as the state variable. Similarly, $\Delta u_{C34} = u_{C3}$-u_{C4} is utilized as the output side voltage control variable. Consequently, TLNBC can be modeled using the variables i_L, Δu_{C12}, and Δu_{C34}.

Without loss of generality, the operating range of $-1 \le D \le (M\text{-}1)/2$ in Buck mode, $-M \le D \le 0$ in Buck–Boost mode and $M \le D \le (1\text{-}M)/2$ in Boost mode in Table I are selected. The operating time of each state in different modes is shown in Table III.

Based on the circuit states and their corresponding operation times presented in Table III, the average state equations for the Buck, Buck–Boost, and Boost modes can be derived, as shown in

$$\frac{\mathrm{d}}{\mathrm{d}t}\begin{bmatrix} i_L \\ \Delta u_{C12} \\ \Delta u_{C34} \end{bmatrix} = \begin{bmatrix} 0 & \frac{d_{11}-d_{14}}{2L} & 0 \\ \frac{d_{14}-d_{11}}{C_1} & 0 & 0 \\ 0 & 0 & 0 \end{bmatrix}\begin{bmatrix} i_L \\ \Delta u_{C12} \\ \Delta u_{C34} \end{bmatrix} + \begin{bmatrix} \frac{d_{11}+d_{14}}{2L} & -\frac{1}{L} \\ 0 & 0 \\ 0 & 0 \end{bmatrix}\begin{bmatrix} u_i \\ u_o \end{bmatrix} \tag{6}$$

$$\frac{\mathrm{d}}{\mathrm{d}t}\begin{bmatrix} i_L \\ \Delta u_{C12} \\ \Delta u_{C34} \end{bmatrix} = \begin{bmatrix} 0 & \frac{d_{11}-d_{14}}{2L} & \frac{d_{22}-d_{23}}{2L} \\ \frac{d_{14}-d_{11}}{C_1} & 0 & 0 \\ \frac{d_{22}-d_{23}}{C_3} & 0 & 0 \end{bmatrix}\begin{bmatrix} i_L \\ \Delta u_{C12} \\ \Delta u_{C34} \end{bmatrix} + \begin{bmatrix} \frac{d_{11}+d_{14}}{2L} & \frac{d_{22}+d_{23}-2}{2L} \\ 0 & 0 \\ 0 & 0 \end{bmatrix}\begin{bmatrix} u_i \\ u_o \end{bmatrix} \tag{7}$$

$$\frac{\mathrm{d}}{\mathrm{d}t}\begin{bmatrix} i_L \\ \Delta u_{C12} \\ \Delta u_{C34} \end{bmatrix} = \begin{bmatrix} 0 & 0 & \frac{d_{22}-d_{23}}{2L} \\ 0 & 0 & 0 \\ \frac{d_{23}-d_{22}}{C_3} & 0 & 0 \end{bmatrix}\begin{bmatrix} i_L \\ \Delta u_{C12} \\ \Delta u_{C34} \end{bmatrix} + \begin{bmatrix} \frac{1}{L} & \frac{d_{22}+d_{23}-2}{2L} \\ 0 & 0 \\ 0 & 0 \end{bmatrix}\begin{bmatrix} u_i \\ u_o \end{bmatrix}. \tag{8}$$

The operation time of TLNBC in other duty ratio ranges can be obtained using the above analysis method, and combined with the state equations, we can have the same converter model, and will not be repeated here.

B. Multiobjective Decoupling MPC Strategy

By discretizing (6)–(8), we obtain the discrete expressions of the control variables in Buck, Buck–Boost, and Boost modes, as shown in

$$\begin{cases} i_L^{k+1} = i_L^k + \frac{T_S}{2L}\left[(d_{11}+d_{14})\,u_i^k - 2u_o^k + (d_{11}-d_{14})\,\Delta u_{C12}^k\right] \\ \Delta u_{C12}^{k+1} = \Delta u_{C12}^k + \frac{T_S}{C_1}(d_{14}-d_{11})\,i_L^k \end{cases} \tag{9}$$

$$\begin{cases} i_L^{k+1} = i_L^k + \frac{T_S}{2L}\left[(d_{11}+d_{14})\,u_i^k + (d_{22}+d_{23}-2)\,u_o^k \right. \\ \qquad \left. + (d_{11}-d_{14})\,\Delta u_{C12}^k + (d_{22}-d_{23})\,\Delta u_{C34}^k\right] \\ \Delta u_{C12}^{k+1} = \Delta u_{C12}^k + \frac{T_S}{C_1}(d_{14}-d_{11})\,i_L^k \\ \Delta u_{C34}^{k+1} = \Delta u_{C34}^k + \frac{T_S}{C_3}(d_{23}-d_{22})\,i_L^k \end{cases} \tag{10}$$

$$\begin{cases} i_L^{k+1} = i_L^k + \frac{T_S}{2L}\left[2u_i^k + (d_{22}+d_{23}-2)\,u_o^k \right. \\ \qquad \left. + (d_{22}-d_{23})\,\Delta u_{C34}^k\right] \\ \Delta u_{C34}^{k+1} = \Delta u_{C34}^k + \frac{T_S}{C_3}(d_{23}-d_{22})\,i_L^k \end{cases} \tag{11}$$

where the symbols marked with k, and k+1 represent current sampling value and predicted value, respectively.

From (9)–(11) it can be seen that there is a coupling relationship between system current and split capacitor voltage, which mutually influence each other. The commonly employed strategy for voltage balancing is to overlay the duty ratio generated by the independent voltage balancing closed-loops onto the main duty ratio, enabling concurrent control of current and capacitor voltage balancing. Consequently, the operational characteristics of system current, considering the superimposed duty ratio and adhering to the voltage balancing duty ratio constraints, are illustrated in Fig. 8.

As shown in Fig. 8, the main duty ratio under superimposed duty ratio control has a significant control effect on the current, while the duty ratio generated by the voltage balancing closed-loop primarily influences the current ripple. Based on this principle, the primary current control duty ratios are denoted

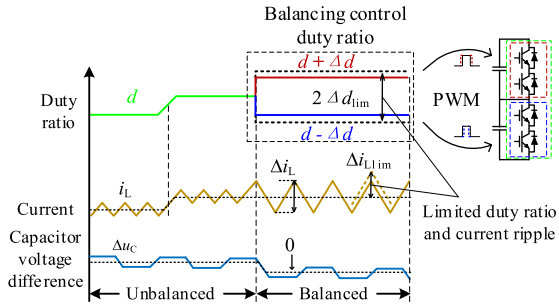

Fig. 8. Current ripple characteristics under duty ratio superposition control.

as $d_1{}^{\mathrm{k}}$ and $d_2{}^{\mathrm{k}}$, with $d_1{}^{\mathrm{k}}$ controlling S_{11} and S_{23}, and $d_2{}^{\mathrm{k}}$ controlling S_{14} and S_{22}. Duty ratios used to achieve voltage balance control are defined as $\Delta d_{\mathrm{C12}}{}^{\mathrm{k}}$ and $\Delta d_{\mathrm{C34}}{}^{\mathrm{k}}$. Given that the carrier offset solely influences the operating range of Buck–Boost mode, a specific value is assigned to M, set as 0.2, in the subsequent discourse. Consequently, according to the basic operating principle of dual-carrier modulation, the duty ratios can be derived, as elucidated in

$$\begin{cases} d_{11}^k = d_1^k + \Delta d_{C12}^k & \text{if } (d_{ij}^k \le 0), d_{ij}^k = 0 \\ d_{14}^k = d_2^k - \Delta d_{C12}^k & \text{if } (d_{ij}^k \ge 1), d_{ij}^k = 1 \\ d_{22}^k = d_2^k - \frac{2}{3} + \Delta d_{C34}^k & i = 1, 2 \\ d_{23}^k = d_1^k - \frac{2}{3} - \Delta d_{C34}^k & j = 1, 2, 3, 4 \end{cases} \tag{12}$$

2/3 is the duty ratio difference generated by carrier offset when $M = 0.2$. According to Fig. 8 and (12), when ignoring the impact of ripple changes on the average current, the control of i_{L}, Δu_{C12}, and Δu_{C34} can be approximately treated as independent, thus, the following cost functions can be defined for the MOD-MPC strategy to control TLNBC:

$$\begin{cases} J_L^k = \left(i_L^* - i_L^{k+1}\right)^2 \\ J_{C12}^k = \left(\Delta u_{C12}^* - \Delta u_{C12}^{k+1}\right)^2 \\ J_{C34}^k = \left(\Delta u_{C34}^* - \Delta u_{C34}^{k+1}\right)^2 \end{cases} \tag{13}$$

where the symbol marked with $*$ represents the reference value. Taking the Buck–Boost mode as an example, substituting (10) into (12) yields the predicted current as follows:

$$\begin{aligned} i_L^{k+1} = i_L^k + \frac{T_S}{2L}[&(d_1^k + d_2^k)u_i^k + (d_1^k + d_2^k - \frac{10}{3})u_o^k \\ &+ (d_1^k - d_2^k + 2\Delta d_{C12}^k)\Delta u_{C12}^k \\ &+ (d_2^k - d_1^k + 2\Delta d_{C34}^k)\Delta u_{C34}^k]. \end{aligned} \tag{14}$$

Because the voltage difference between the series split capacitors under steady-state is small, thus, $\Delta d_{\mathrm{C12}}{}^{\mathrm{k}}$ and $\Delta d_{\mathrm{C34}}{}^{\mathrm{k}}$ can be ignored. By combining the current cost function in (13) with (14), the function of $J_L{}^k$ with respect to $d_1{}^{\mathrm{k}}$ and $d_2{}^{\mathrm{k}}$ can be obtained. Taking the partial derivatives of $J_L{}^k$ for $d_1{}^{\mathrm{k}}$ and $d_2{}^{\mathrm{k}}$, respectively, we can have

$$\begin{cases} \left.\frac{\partial J_L^k}{\partial d_1^k}\right|_{d_2^k=1} = 2\left(\frac{\partial i_L^*}{\partial d_1^k} - \frac{\partial i_L^{k+1}}{\partial d_1^k}\right)\left(i_L^* - i_L^{k+1}\right) \\ \left.\frac{\partial J_L^k}{\partial d_2^k}\right|_{d_1^k=1} = 2\left(\frac{\partial i_L^*}{\partial d_2^k} - \frac{\partial i_L^{k+1}}{\partial d_2^k}\right)\left(i_L^* - i_L^{k+1}\right). \end{cases} \tag{15}$$

According to the Lagrange multiplier method and (13), it can be concluded that when $d_1{}^{\mathrm{k}} = 1$ and $d_2{}^{\mathrm{k}} = 1$, the partial derivative of $J_L{}^k$ reaches the minimum value [25]. At this moment, the optimal d_1 and d_2 for current regulation at time k can be obtained by combining (14), as shown in

$$\begin{aligned} d_1^k = &\frac{2L(i_L^* - i_L^k)}{T_S(u_i^k + u_o^k + \Delta u_{C12}^k - \Delta u_{C34}^k)} \\ &- \frac{u_i^k - \frac{7}{3}u_o^k - \Delta u_{C12}^k + \Delta u_{C34}^k}{u_i^k + u_o^k + \Delta u_{C12}^k - \Delta u_{C34}^k} \end{aligned} \tag{16}$$

$$\begin{aligned} d_2^k = &\frac{2L(i_L^* - i_L^k)}{T_S(u_i^k + u_o^k - \Delta u_{C12}^k + \Delta u_{C34}^k)} \\ &- \frac{u_i^k - \frac{7}{3}u_o^k + \Delta u_{C12}^k - \Delta u_{C34}^k}{u_i^k + u_o^k - \Delta u_{C12}^k + \Delta u_{C34}^k}. \end{aligned} \tag{17}$$

When the system reaches steady states and the split capacitor voltage is balanced, $\Delta u_{\mathrm{C12}}{}^{\mathrm{k}} = \Delta u_{\mathrm{C34}}{}^{\mathrm{k}} = 0$, and $d_1{}^{\mathrm{k}} = d_2{}^{\mathrm{k}}$. However, if the capacitor voltage is not balanced, further adjustments to the final duty ratio are required because the cost function only constrains system current.

As the operating circuits shown in Table I, when TLNBC operates in Buck–Boost mode, $\Delta d_{\mathrm{C12}}{}^{\mathrm{k}}$ and $\Delta d_{\mathrm{C34}}{}^{\mathrm{k}}$ control the capacitor voltage at both sides, separately. Substituting the voltage balancing duty ratio in (10) into (12), the predicted value of the input side capacitor voltage difference can be derived

$$\Delta u_{C12}^{k+1} = \Delta u_{C12}^k + \frac{T_S}{C_1}\left(d_2^k - d_1^k - 2\Delta d_{C12}^k\right) i_L^k. \tag{18}$$

According to the input side capacitor voltage cost function in (13) and (18), we can obtain the function $J_{\mathrm{C12}}{}^k$ with respect to $d_{\mathrm{C12}}{}^{\mathrm{k}}$. Taking Δd_{C12} derivative of $J_{\mathrm{C12}}{}^k$, we can have

$$\frac{\mathrm{d}J_{C12}^k}{\mathrm{d}d_{C12}^k} = 2\left(\frac{\mathrm{d}u_{C12}^*}{\mathrm{d}d_{C12}^k} - \frac{\mathrm{d}u_{C12}^{k+1}}{\mathrm{d}d_{C12}^k}\right)\left(u_{C12}^* - u_{C12}^{k+1}\right). \tag{19}$$

When the voltage difference between the split capacitors is zero, it indicates that the series split capacitors have reached the balanced state. At this moment, $J_{\mathrm{C12}}{}^k$ reaches its extreme value. By combining (18), we can derive the expression for the optimal value of Δd_{C12} at time k

$$\Delta d_{C12}^k = \frac{1}{2}d_1^k - \frac{1}{2}d_2^k + \frac{C_1\Delta u_{C12}^k}{2T_S \cdot i_L^k}. \tag{20}$$

Because of the symmetrical structure of the converter, the expression for Δd_{C34} on the other side can be obtained as follows:

$$\Delta d_{C34}^k = \frac{1}{2}d_1^k - \frac{1}{2}d_2^k + \frac{C_3\Delta u_{C34}^k}{2T_S \cdot i_L^k}. \tag{21}$$

As mentioned earlier, the assumption in (12) is that the voltage balancing duty ratio only affects the current ripple. Therefore, constraints need to be set on (20) and (21) to minimize the impact of current ripple on the average current. It can be seen from Fig. 8 that when the duty ratios in (20) and (21) are limited within Δd_{lim}, the maximum current ripple will not exceed $2\Delta i_{\mathrm{Llim}}$. Thus, by combining it with the inductor voltage equation, the expression for Δd_{lim} can be deduced, as shown in (22). In

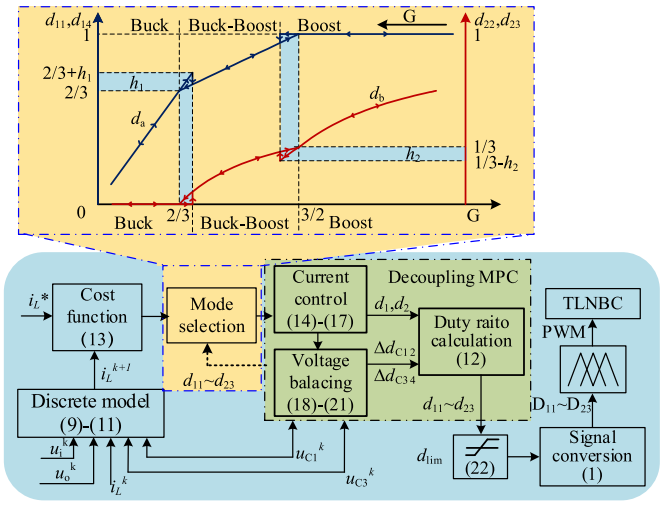

Fig. 9. Control block diagram of the proposed MPC strategy.

practice, a larger $\Delta d_{\lim}$ can enhance the voltage balancing response speed, but it will also increase the current ripple

$$\Delta d_{\lim} = \pm \frac{L}{T_S}\left(\frac{4\Delta_{L\lim} - 2\Delta i_L}{u_o^* - u_i^k}\right). \tag{22}$$

Thus, substituting (16), (17), (20), and (21), respectively, into (12), the final duty ratio to control TLNBC based MPC can be derived, which is decoupled. In comparison to the iterative optimization method employed in traditional MPC strategy, the proposed MOD-MPC strategy efficiently reduces the computational burden of the controller by obtaining the duty ratio through straightforward calculations. The overall control block diagram of the proposed MPC strategy is shown in Fig. 9.

Although the converters have a similar voltage gain at the mode switching point, frequent mode switching near the switching point can occur. To address this issue, a duty ratio hysteresis is introduced at the mode switching point, as illustrated in Fig. 9. Here, d_a is the larger one between d_{11} and d_{14}, and d_b is smaller one between d_{22} and d_{23}, h_1 and h_2 are the hysteresis width.

C. Stability Analysis

Direct Lyapunov method is employed in the article to verify the stability of MOD-MPC strategy. Direct Lyapunov method indicates that when the function $V(\mathbf{x})$ defined according to the system state variables $\mathbf{x}$ satisfies that $V(\mathbf{x})$ is positive, $\dot{V}(\mathbf{x})$is negative and $\lim_{\|\mathbf{x}\|\to\infty} V(\mathbf{x}) = \infty$, thus, the system is stable [26], [27], [28]. So, according to the cost function, the discrete Lyapunov function can be defined as follows:

$$V(\mathbf{x})^k = [\mathbf{x}^k - \mathbf{x}^*]^T[\mathbf{x}^k - \mathbf{x}^*] \tag{23}$$

where $\mathbf{x}$ represents the system control variables $[i_L \Delta u_{C12} \Delta u_{C34}]^T$.

According to (10) and (23), the change rate of Lyapunov function can be expressed as

$$\begin{aligned}\Delta V(i_L)^k &= V(i_L)^{k+1} - V(i_L)^k \\ &= \left|i_L^k + \frac{T_S}{2L}\left[(d_1^k - d_2^k)\Delta u_{C12}^k + (d_2^k - d_1^k)\Delta u_{C34}^k\right.\right. \\ &\quad \left.\left. + (d_1^k + d_2^k)u_i^k + (d_1^k + d_2^k - \frac{10}{3})u_o^k\right] - i_L^*\right|^2 \\ &\quad - [i_L^k - i_L^*]^T[i_L^k - i_L^*] \end{aligned} \tag{24}$$

$$\begin{aligned}\Delta V(\Delta u_{Cj})^k &= V(\Delta u_{Cj})^{k+1} - V(\Delta u_{Cj})^k \\ &= \left|\Delta u_{Cj}^k + \frac{T_S}{C_j}(d_2^k - d_1^k)i_L^k - \Delta u_{Cj}^*\right|^2 \\ &\quad - [\Delta u_{Cj}^k - \Delta u_{Cj}^*]^T[\Delta u_{Cj}^k - \Delta u_{Cj}^*] \end{aligned} \tag{25}$$

where $j = 12, 34$.

When the duty ratio is within the limit, the dynamic characteristics of MPC yield the following results from (16), (17), (20), and (21):

$$\begin{cases} i_L^* \approx i_L^k + \frac{T_S}{2L}[(d_1^k + d_2^k)u_i^k + (d_1^k + d_2^k - \frac{10}{3})u_o^k \\ \quad + (d_1^k - d_2^k)\Delta u_{C12}^k + (d_2^k - d_1^k)\Delta u_{C34}^k] \\ \Delta u_{Cj}^* \approx \Delta u_{Cj}^k + \frac{T_S}{C_j}(d_2^k - d_1^k)i_L^k. \end{cases} \tag{26}$$

Substituting (26) into (24) and (25), respectively, yields

$$\begin{cases} \Delta V(i_L)^k = -\left|i_L^k - i_L^*\right|^2 \\ \Delta V(\Delta u_{Cj})^k = -\left|\Delta u_{Cj}^k - \Delta u_{Cj}^*\right|^2. \end{cases} \tag{27}$$

However, the final duty ratio may not reach the desired value due to the limited duty ratio, causing the predicted value to fail to track the reference. So, the duty ratio needs to be adjusted according to the variation of ΔV(x) to ensure stable and convergent control of the variable. Incorporating (23), the duty ratio limiting is defined as follows:

$$\Delta d_{\lim}^k = \begin{cases} \pm\left(\left|\Delta d_{\lim}^{k-1}\right| + c_n\right), \text{if } \triangle V(x)^k > 0 \\ \pm\frac{L}{T_S}\left(\frac{4\Delta i_{L\lim} - 2\Delta i_L}{u_o^* - u_i^k}\right), \text{if } \triangle V(x)^k \le 0 \end{cases} \tag{28}$$

where c_n is a constant that represents the magnitude of the change in the duty ratio limiting. When the converter operates at the mode switching point, although $V(\mathbf{x})^{k+1}$ and $V(\mathbf{x})^k$ are in different operating modes, the predicted value always tracks the reference value, thus (27) always holds. Therefore, according to (23) and (27), and Lyapunov stability criterion, the system is globally stable.

IV. Experimental Verification

To validate the performance of the proposed MPC strategy, an experimental platform is built in the laboratory, as shown in Fig. 10. The platform incorporates a dual-core control architecture, combining TMS320F28335 and XC3S500E. TMS320F28335 is responsible for sampling and real-time calculations, while XC3S500E is dedicated to generating PWM signals and ensuring the system's overall protection. This integrated setup provides a robust and reliable testing environment for evaluating the performance of the MPC power balancing strategy. The detailed experimental parameters are shown in Table IV. The experiment consists of five parts: verification of dual-carrier modulation, validation of MOD-MPC in different

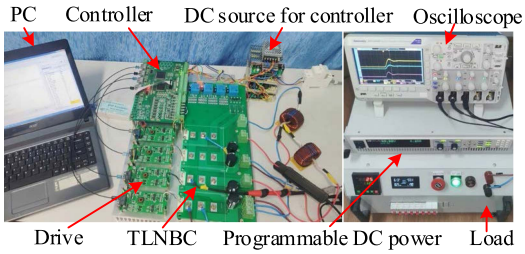

Fig. 10. Experimental platform.

TABLE IV
EXPERIMENTAL PARAMETERS

Item	Value	Unit
Input voltage	48	V
Output voltage range	20–100	V
Switching frequency	10	kHz
Split capacitor on input side	470	μF
Split capacitor on output side	470	μF
Loop inductance	1	mH
Critical voltage between Buck and Buck–Boost mode	32	V
Critical voltage between Buck–Boost and Boost mode	72	V
Load	20	Ω
Maximum operating power	1000	W

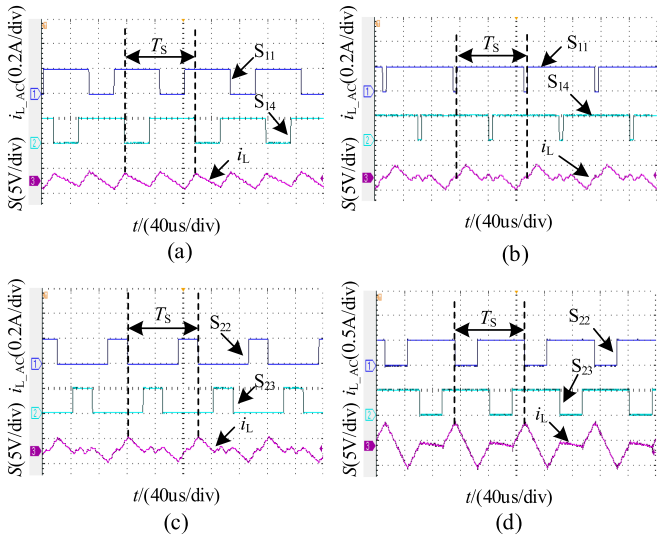

Fig. 11. Drive signals and current waveform. (a) Buck mode. (b) Buck–Boost mode. (c) Buck–Boost mode. (d) Boost mode.

modes, verification under abrupt load changing, validation of port voltage slow variation, and comparison with the traditional strategy. The specific experimental results are as follows.

A. Experiment I: Basic Operating Characteristic

The current ripple curves in different operating modes are shown in Fig. 11. Specifically, Fig. 11(a) and (d) depicts the current curves in Buck and Boost modes, respectively. In the Buck mode, the switching devices S_{22} and S_{23} are in the OFF state, while in the Boost mode, the devices S_{11} and S_{14} are in the ON state. On the other hand, Fig. 11(b) and (c), respectively,

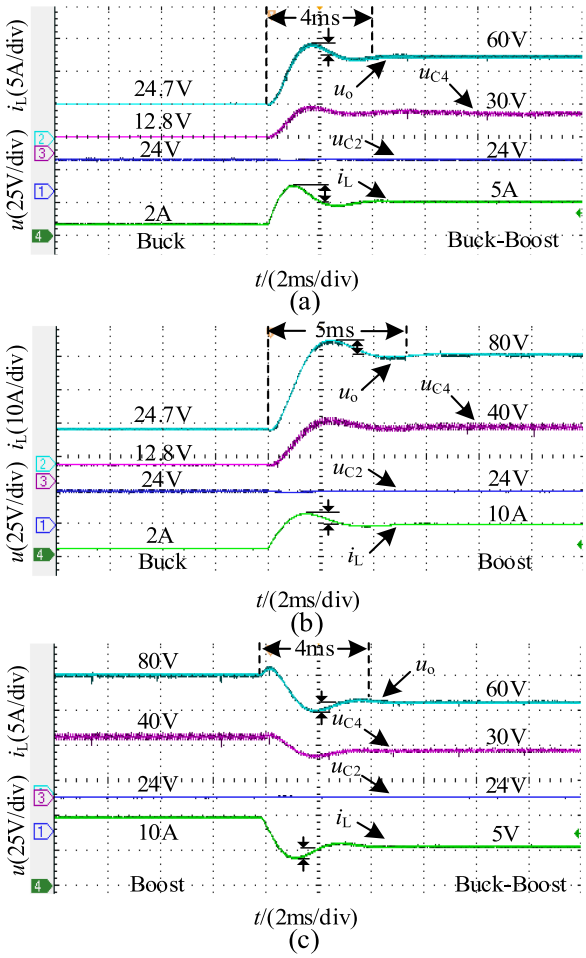

Fig. 12. Control performance verification of MOD-MPC. (a) Transition from Buck mode to Buck–Boost mode (b) Transition from Buck mode to Boost mode. (c) Transition from Boost mode to Buck–Boost mode.

depicts the inductor current waveforms of the converter operating in the Buck–Boost mode when the output voltage decreases and increases. As can be observed, the ripple frequency is always twice the switching frequency, indicating that the TLNBC operates with three levels in all modes.

B. Experiment II: Effectiveness of MOD-MPC in Different Modes

The verification results of current and voltage balancing control of the proposed MOD-MPC strategy with dual-carrier modulation are shown in Fig. 12. The inductor current reference undergoes a step change from 2 A to 5 A and the output voltage steps from 24.7 V to 60 V in Fig. 12(a), the converter switches from Buck to Buck–Boost mode. It takes approximately 4 ms for u_o, u_{C4}, and i_L to stabilize, while u_{C2} remains constant due to the unchanged input voltage. Similarly, in Fig. 12(b), where the inductor current reference steps from 2 A to 10 A and the output voltage steps from 24.7 V to 80 V, the converter transitions from Buck to Boost mode. The stabilization of u_o, u_{C4}, and i_L is achieved within 5 ms. Furthermore, when the inductor current reference changes from 10 A to 5 A in Fig. 12(c), the

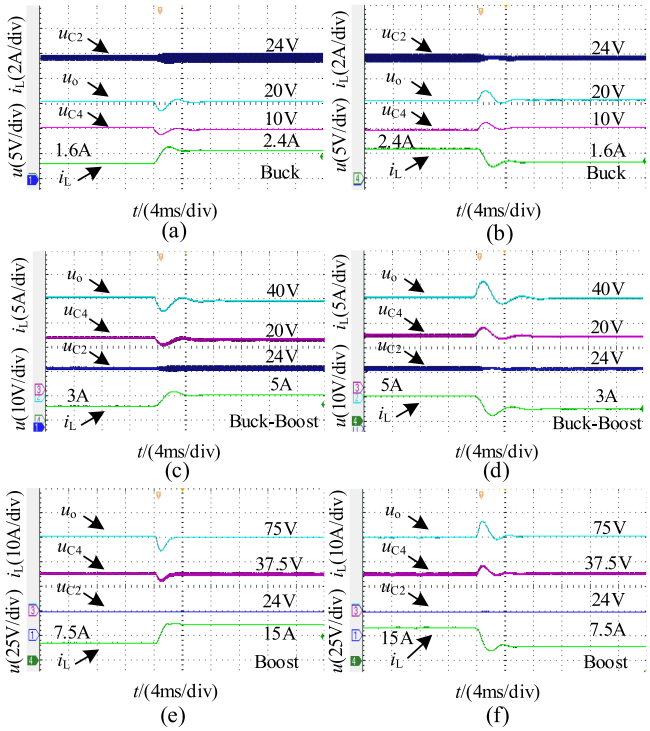

Fig. 13. Experimental results with load variation. (a) Load in Buck mode. (b) Unload in Buck mode. (c) Load in Buck–Boost mode. (d) Unload in Buck–Boost mode. (e) Load in Boost mode. (f) Unload in Boost mode.

converter switches from Boost to Buck–Boost mode, and the stabilization of u_o, u_{C4}, and i_L is achieved within about 4 ms. The experimental results show that the proposed MOD-MPC has favorable current and voltage balancing control capabilities and dynamic response performance in Buck, Buck–Boost, and Boost modes, and can achieve smooth switching of operating modes.

C. Experiment III: Abruptly Load Changing

The dynamic response of the TLNBC under abrupt load changing is depicted in Fig. 13. Fig. 13(a) and (b) presents the waveform when subjected to sudden load increase and load decrease, respectively, with $u_o = 20$ V in Buck mode. It is discernible that during load transitions, the output voltage undergoes a transient fluctuation of approximately 10%, returning to its steady state after approximately 6 ms. Concurrently, the inductor current stabilizes during this period.

Similarly, the load transient response waveforms are evident in the Buck–Boost mode depicted in Fig. 13(c) and (d), as well as the Boost mode illustrated in Fig. 13(e) and (f). The graphical representations demonstrate that both u_o and i_L exhibit a recovery period to stability within 6 ms, characterized by overshoots of less than 20%. Furthermore, the capacitor voltage maintains a balanced state at half the port voltage. The above experimental results indicate that the proposed MOD-MPC can respond quickly in Buck, Buck–Boost, and Boost modes when the load abruptly changes, and has favorable system current and capacitor voltage balancing control capabilities.

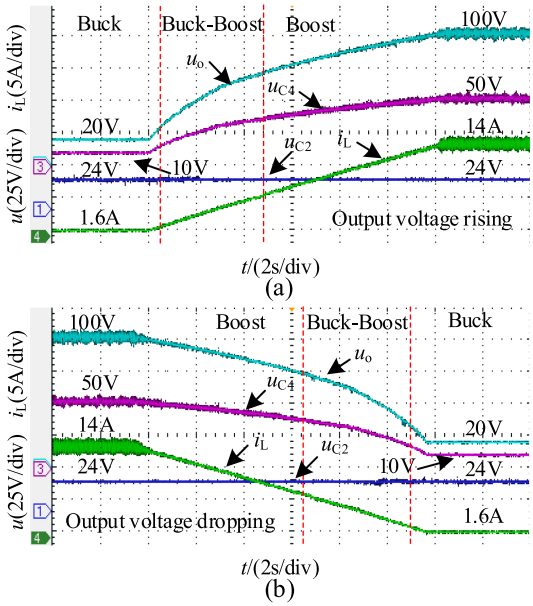

Fig. 14. Experimental results with gradual output voltage variation. (a) Output voltage increase. (b) Output voltage decrease.

D. Experiment IV: System Response Under Gradual Output Voltage Variation

The operational process of TLNBC during gradual variations of port voltages is illustrated in Fig. 14. Fig. 14(a) illustrates the gradual increase in output voltage, depicting the converter's output voltage ascending from 20 V to 100 V over 12 s. It can be observed that during the voltage variation, the voltage of C_4 consistently maintains half of the output voltage, while the voltage of C_2 remains constant. Simultaneously, the inductor current increases from 1.6 A to 14 A, which is controllable. Similarly, Fig. 14(b) illustrates the process of continuous decrease in output voltage, where u_o, u_{C4}, and i_L undergo continuous changes until reaching a steady state over the 12 s period.

It can be observed from Fig. 14 that the proposed MPC strategy exhibits favorable control performance for gradual variation of output voltage. Meanwhile, the proposed MPC strategy ensures a smooth transition of the converter in Buck, Buck–Boost, and Boost operating modes.

E. Experiment V: Comparative Verification

In order to further validate the superior dynamic response characteristics of the proposed strategy, a traditional controller designed with PI algorithm, as referenced in [19], was implemented. As illustrated in Fig. 15, the control block diagram outlines the design of the current loop utilizing a PI controller for effective system current control. Furthermore, it integrates voltage balancing loops with PI controllers to ensure balanced control of the split capacitors.

According to the strategy shown in Fig. 15, the experimental results of TLNBC can be obtained, as shown in Fig. 16. The inductor current reference undergoes a step change from 2 A to 5 A and the output voltage steps from 24.7 V to 60 V in Fig. 16(a).

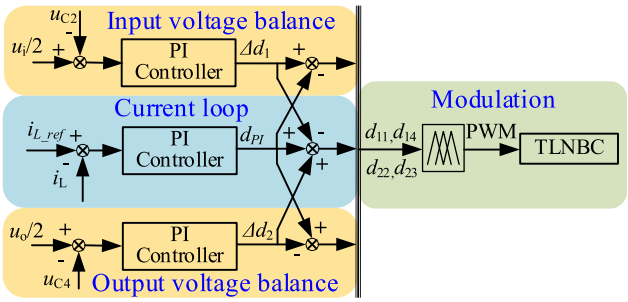

Fig. 15. Control strategy block diagram based on PI algorithm.

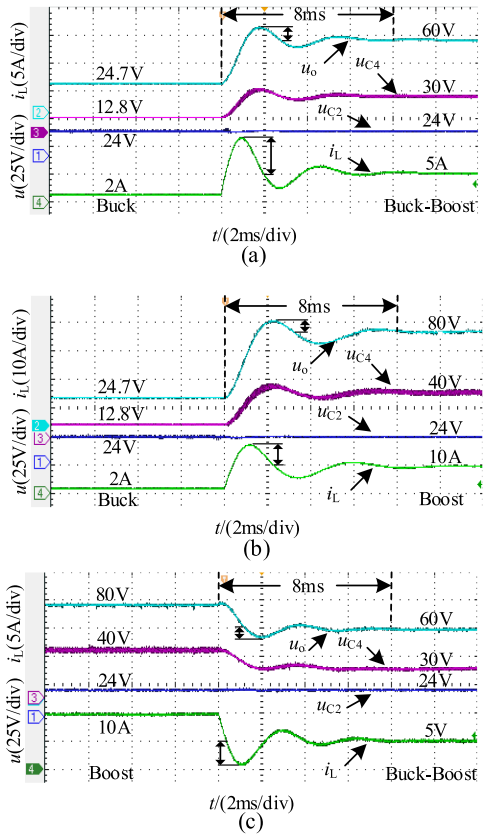

Fig. 16. Control performance verification of traditional PI strategy. (a) Transition from Buck mode to Buck–Boost mode. (b) Transition from Buck mode to Boost mode. (c) Transition from Boost mode to Buck–Boost mode.

The converter operates from Buck to Buck–Boost mode, and the response time is approximately 8 ms. Similarly, from Fig. 16(b), it can be observed that the inductor current steps from 2 A to 10 A, the output voltage steps from 24.7 V to 80 V, and the converter switches from Buck to Boost mode. It reaches a steady state after approximately 8 ms. Furthermore, when the inductor current reference changes from 10 A to 5 A in Fig. 16(c), the converter switches from Boost to Buck–Boost mode. The system requires about 8ms to reach steady state. Compared with the experimental results shown in Fig. 12 under the same operating conditions, the MOD-MPC strategy proposed in the article has faster response speed and better current control performance.

V. Conclusion

This article proposes a MOD-MPC strategy based on dual-carrier modulation for TLNBC in dc ESS to solve the bidirectional power control problem when the voltage changes on the dc bus side and battery side. A simplified modeling method for TLNBC based on split capacitor voltage difference is the proposed. On this basis, a MOD-MPC control strategy based on dual-carrier modulation is proposed to effectively control system current and split capacitor voltage, and the optimization of solving cost functions is studied to reduce the computational load. Experimental results demonstrate that the proposed MOD-MPC strategy based on dual-carrier modulation ensures efficient control of system current and split capacitor voltage of TLNBC under continuous adjustable operating modes, making it suitable for applications in dc ESS.

Reference

[1] K. Sun, L. Zhang, Y. Xing, and J. M. Guerrero, "A distributed control strategy based on DC bus signaling for modular photovoltaic generation systems with battery energy storage," *IEEE Trans. Power Electron.*, vol. 26, no. 10, pp. 3032–3045, Oct. 2011.

[2] S. M. Taheri, A. Baghramian, and S. A. Pourseyedi, "A novel high-step-up sepic-based non isolated three-port DC-DC converter proper for renewable energy applications," *IEEE Trans. Ind. Electron.*, vol. 70, no. 10, pp. 10114–10122, Oct. 2023.

[3] Q. Tian, G. Zhou, L. Wang, Q. Bi, and M. Leng, "Symmetric bipolar output full-bridge four-port converter with phase-shift modulated buck-boost voltage balancer," *IEEE Trans. Ind. Electron.*, vol. 69, no. 8, pp. 8040–8054, Aug. 2022.

[4] L. Wang, H. Wang, M. Fu, J. Liang, and Y. Liu, "A three-port energy router for grid-tied PV generation systems with optimized control methods," *IEEE Trans. Power Electron.*, vol. 38, no. 1, pp. 1218–1231, Jan. 2023.

[5] N. Hou and Y. Li, "Communication-free power management strategy for the multiple DAB-based energy storage system in islanded DC microgrid," *IEEE Trans. Power Electron.*, vol. 36, no. 4, pp. 4828–4838, Apr. 2021.

[6] J. Fang, Y. Tang, H. Li, and X. Li, "A battery/ultracapacitor hybrid energy storage system for implementing the power management of virtual synchronous generators," *IEEE Trans. Power Electron.*, vol. 33, no. 4, pp. 2820–2824, Apr. 2018.

[7] J. Wang, K. Sun, C. Xue, T. Liu, and Y. Li, "Multi-port DC-AC converter with differential power processing DC-DC converter and flexible power control for battery ESS integrated PV systems," *IEEE Trans. Ind. Electron.*, vol. 69, no. 5, pp. 4879–4889, May 2022.

[8] H.-S. Lee and J.-J. Yun, "High-efficiency bidirectional buck-boost converter for photovoltaic and energy storage systems in a smart grid," *IEEE Trans. Power Electron.*, vol. 34, no. 5, pp. 4316–4328, May 2019.

[9] H. Watanabe, T. Sakuraba, K. Furukawa, K. Kusaka, and J.-I. Itoh, "Development of DC to single-phase AC voltage source inverter with active power decoupling based on flying capacitor DC/DC converter," *IEEE Trans. Power Electron.*, vol. 33, no. 6, pp. 4992–5004, Jun. 2018.

[10] P. J. Grbovic, P. Delarue, P. L. Moigne, and P. Bartholomeus, "A bidirectional three-level DC-DC converter for the ultracapacitor applications," *IEEE Trans. Ind. Electron.*, vol. 57, no. 10, pp. 3415–3430, Oct. 2010.

[11] K. Bi et al., "A model predictive controlled bidirectional four quadrant flying capacitor DC/DC converter applied in energy storage system," *IEEE Trans. Power Electron.*, vol. 37, no. 7, pp. 7705–7717, Jul. 2022.

[12] W. Liu, H. Jin, W. Yao, and Z. Lu, "An interleaved PWM method with better voltage-balancing ability for half-bridge three-level DC/DC converter," *IEEE Trans. Power Electron.*, vol. 33, no. 6, pp. 4594–4598, Jun. 2018.

[13] U. Manandhar, B. Wang, X. Zhang, G. H. Beng, Y. Liu, and A. Ukil, "Joint control of three-level DC-DC converter interfaced hybrid energy storage system in DC microgrids," *IEEE Trans. Energy Convers.*, vol. 34, no. 4, pp. 2248–2257, Dec. 2019.

[14] S. Rivera and B. Wu, "Electric vehicle charging station with an energy storage stage for split-DC bus voltage balancing," *IEEE Trans. Power Electron.*, vol. 32, no. 3, pp. 2376–2386, Mar. 2017.

[15] K. Bi, Y. Lu, Y. Zhuang, Y. Zhu, and Q. Fan, "Decoupling power balancing strategy with reduced current sensors for two-phase interleaved neutral point clamped DC/DC converter applied in energy storage system," *IEEE Trans. Energy Convers.*, vol. 38, no. 1, pp. 147–157, Mar. 2023.

[16] A. M. Y. M. Ghias, J. Pou, G. J. Capella, V. G. Agelidis, R. P. Aguilera, and T. Meynard, "Single-carrier phase-disposition PWM implementation for multilevel flying capacitor converters," *IEEE Trans. Power Electron.*, vol. 30, no. 10, pp. 5376–5380, Oct. 2015.
[17] Y. Bai, S. Hu, Z. Yang, Z. Zhu, and Y. Zhang, "Model predictive control for Four-Switch buck-boost converter based on tuning-free cost function with smooth mode transition," *IEEE J. Emerg. Sel. Topics Power Electron.*, vol. 10, no. 6, pp. 6607–6618, Dec. 2022.
[18] I. Aharon, A. Kuperman, and D. Shmilovitz, "Analysis of dual-carrier modulator for bidirectional noninverting buck-boost converter," *IEEE Trans. Power Electron.*, vol. 30, no. 2, pp. 840–848, Feb. 2015.
[19] H.-C. Chen, C.-Y. Lu, W.-H. Lien, and T.-H. Chen, "Active capacitor voltage balancing control for three-level flying capacitor boost converter based on average-behavior circuit model," *IEEE Trans. Ind. Appl.*, vol. 55, no. 2, pp. 1628–1638, Mar./Apr. 2019.
[20] J. Rodriguez et al., "Latest advances of model predictive control in electrical drives—Part I: Basic concepts and advanced strategies," *IEEE Trans. Power Electron.*, vol. 37, no. 4, pp. 3927–3942, Apr. 2022.
[21] D. E. Quevedo, R. P. Aguilera, M. A. Perez, P. Cortes, and R. Lizana, "Model predictive control of an AFE rectifier with dynamic references," *IEEE Trans. Power Electron.*, vol. 27, no. 7, pp. 3128–3136, Jul. 2012.
[22] L. M. A. Caseiro, A. M. S. Mendes, and S. M. A. Cruz, "Dynamically weighted optimal switching vector model predictive control of power converters," *IEEE Trans. Ind. Electron.*, vol. 66, no. 2, pp. 1235–1245, Feb. 2019.
[23] F. A. Villarroel et al., "Stable shortest horizon FCS-MPC output voltage control in non-minimum phase boost-type converters based on input-state linearization," *IEEE Trans. Energy Convers.*, vol. 36, no. 2, pp. 1378–1391, Jun. 2021.
[24] H. Chen, D. Wang, S. Tang, X. Yin, J. Wang, and Z. J. Shen, "Continuous control set model predictive control for three-level flying capacitor boost converter with constant switching frequency," *IEEE J. Emerg. Sel. Topics Power Electron.*, vol. 9, no. 5, pp. 5996–6007, Oct. 2021.
[25] J. Liao, G. Qiu, Y. Huang, and V. Khadkikar, "Lagrange multiplier based control method to optimize efficiency for four-switch buck-boost converter over whole operating range," *IEEE Trans. Ind. Electron.*, vol. 71, no. 1, pp. 822–833, Jan. 2024.
[26] H. Makhamreh, M. Trabelsi, O. Kukrer, and H. Abu-Rub, "A lyapunov-based model predictive control design with reduced sensors for a PUC7 rectifier," *IEEE Trans. Ind. Electron.*, vol. 68, no. 2, pp. 1139–1147, Feb. 2021.
[27] M. P. Akter, S. Mekhilef, N. M. L. Tan, and H. Akagi, "Modified model predictive control of a bidirectional AC-DC converter based on lyapunov function for energy storage systems," *IEEE Trans. Ind. Electron.*, vol. 63, no. 2, pp. 704–715, Feb. 2016.
[28] J.-J. E. Slotine and W. Li, *Applied Nonlinear Control*, vol. 199, no. 1, Englewood Cliffs, NJ, USA: Prentice-Hall, 1991, p. 705.

Kaitao Bi received and the M.S. and Ph.D. degrees in electrical engineering from the Harbin Institute of Technology, Harbin, China, in 2014 and 2019, respectively.

Since 2019, he has been with Jiangnan University, Wuxi, China, where he is currently an Associate Professor with the School of Internet of Things Engineering. His areas of research interests include multilevel converters, dc–dc converters, high-power energy storage systems, and control algorithms.

Cheng Xu received the B.S. degree in electrical engineering and automation in 2020 from the School of Jiangnan University, Wuxi, China, where since 2021, he has been working toward the M.S. degree in electrical engineering.

His research interests include new energy power conversion system, multilevel converters, and control technologies.

Jian Ai received the Ph.D. degree in electrical engineering from Southeast University, Nanjing, China, in 2021.

In 2022, he was with Jiangnan University, Wuxi, China, where he is currently an Associate Professor with the School of Internet of Things Engineering. Since 2022, he was a Postdoctoral Fellow with the Department of Electrical Engineering, Nanjing University of Aeronautics and Astronautics, Nanjing, China. His current research interests include resonant converters and dc–dc converters.

Jianfei Li received the B.S. and M.S. degrees in electrical engineering from Huazhong University of Science and Technology, Wuhan, China, in 1996 and 1999, respectively.

He is currently the Vice President with Sineng Electric Company Ltd., Wuxi, China, and a master supervisor with the School of Internet of Things, Jiangnan University, Wuxi, China. His main research interests include photovoltaic generation technologies, energy storage system, and distributed generation systems.

Qigao Fan (Senior Member, IEEE) received the Ph.D. degree in mechatronic engineering from the School of Mechatronic Engineering, China University of Mining Technology, Xuzhou, China, in 2013.

Since 2013, he has been with Jiangnan University, Wuxi, China, where he is currently a Professor with the School of Internet of Things Engineering. From 2018 to 2019, he was a visiting scholar with the Department of Mechanical and Industrial Engineering, University of Toronto. His teaching and research interests include motor control, robotics, renewable generation systems, and IoT technology.